

International Conference on Space Optics—ICSO 2022

Dubrovnik, Croatia

3–7 October 2022

Edited by Kyriaki Minoglou, Nikos Karafolas, and Bruno Cugny,



Operational Lifetime Qualification of Laser Diodes for BECCAL



Operational Lifetime Qualification of Laser Diodes for BECCAL

Karl Häusler*, Ahmad Bawamia, Jos Boschker, Jan M. Baumann, Matthias Dammasch,
Hans Wenzel, Andrea Knigge, Jörg Fricke, Andre Maaßdorf, and Andreas Wicht
Ferdinand-Braun-Institut, Leibniz-Institut für Höchstfrequenztechnik,
Gustav-Kirchhoff-Str. 4, D-12489 Berlin

ABSTRACT

We report on processing, characterization and lifetime qualification of lateral single-mode laser diodes emitting at a wavelength of $\lambda = 1064$ nm. The lasers were designed to meet the specifications for the Bose-Einstein Condensate and Cold Atom Laboratory (BECCAL). Ridge waveguide lasers (RWL) were investigated in aging experiments in order to assess the material quality of the ridge waveguide amplifiers (RWA) used in the BECCAL modules. Both RWA and RWL have a cavity length of $L = 6$ mm and a ridge width of $w = 5$ μm , eventually tapered to 15 μm towards the front facet, yielding an optical power of $P_{\text{op}} = 830$ mW ex facet for ≥ 500 mW into a single mode fiber. A four-lot lifetest with temperatures from $T = 20^\circ\text{C}$ to 30°C and optical powers from $P_{\text{op}} = 1.5$ W to 1.7 W was performed aimed at estimating the parameters of accelerated aging. The thermal activation energy of $E_a = 0.80$ eV and the power stress exponent of $n = 5.45$ were obtained. Due to catastrophic optical damage (COD) at the laser facets, the batch with standard facet passivation failed to meet the specified reliability $R > 99\%$ at the operational time of $t_{\text{op}} = 10,000$ h. Using improved passivation technique by cleaving the laser bars in ultra-high vacuum (UHV) followed by ZnSe epitaxy yields a successful suppression of facet degradation. The reliability of 1064 nm RWLs with improved passivation was estimated to be close to $R = 100\%$ demonstrating the qualification of the RWA for BECCAL.

Keywords: accelerated lifetest, space qualification, facet passivation, 1064 nm, ridge waveguide laser, ridge waveguide amplifier

1. INTRODUCTION

The Bose-Einstein condensate and Cold Atom Laboratory (BECCAL) is a joint venture between DLR and NASA. Its goal is to investigate ultracold rubidium (Rb) and potassium (K) atoms in microgravity on board of the International Space Station (ISS) [1]. BECCAL will open a wide field of research areas to study the basics of quantum mechanics, possible applications as high-fidelity quantum sensors, and it may also contribute to understand the transition from quantum mechanics to general relativity, and the still unknown theory of quantum gravity [2].

Research for BECCAL demands for space qualified laser modules with single mode emission at wavelengths ranging from 764 nm for trapping of cold atoms in a blue-detuned optical trap [3], 767 nm for cooling of K, 780 nm for Rb, up to 1064 nm for an optical dipole trap. Space qualification of components requires quality assurance efforts and stringent control of processes, process flows and materials regarding development and manufacturing. At our institute we have established a long-term experience on space qualification of laser modules deployed in laser communication terminals on the satellite TerraSAR-X, the wind lidar on AEOLUS, or the methane remote sensing instrument on MERLIN, for example [4]. Our expertise includes the product and quality assurance following the stringent requirements for space qualification regarding the development, realization, qualification and small-series manufacturing of laser benches and laser modules. In the following, we summarize our recent activities regarding design, processes, characterization and lifetest of 1064 nm lasers aimed at finding a suited design for semiconductor optical amplifiers that meet the requirements for BECCAL. In the initial phase of bread-board development, we tested several variants with different III-V semiconductor layer structures and lateral waveguides.

*karl.hausler@fbh-berlin.de; phone +49 30 6392 3294; fax +49 30 6392 2602; www.fbh-berlin.de

2. EXPERIMENTAL

2.1 Basic specification and design issues

We designed the semiconductor optical amplifier (SOA) to meet the basic specifications for the 1064 nm laser module, that shall provide an optical output power of 500 mW from a single-mode optical fiber. Inside the module, the SOA is seeded by an external-cavity laser (ECDL) yielding a technical spectral linewidth in the range of 100 kHz. Regarding the worst-case estimate of $\eta_{CE} = 60\%$ for the coupling efficiency, an optical output power of $P = 0.83$ W of the SOA is specified for coupling of the amplified light into the fiber. The modules shall work without failure over the full operational time, which is defined as $t_{op} = 10,000$ hours for this mission. As benchmark for the reliability R , which is probability of failure-free operation, $R(t_{op}) > 99\%$ is demanded. The amplifier design shall be suited to meet those specifications. For the mainly single mode operation, ridge waveguide amplifiers (RWA) are used, some with slightly tapered sections.

The master oscillator power amplifier (MOPA) module includes the ECDL, the RWA, optical isolators and beam forming optics. In terms of reliability, the SOA is the most critical part having the highest power density within the semiconductor active material, which is sensitive to aging. It therefore is reasonable to qualify the RWA material before integrating it into the module. Therefore, the ridge waveguide lasers (RWL) were designed to have identical semiconductor material and lateral dimensions, and they stem from the same processing lots as the RWA. The only differences are the following: the RWA is tilted by an angle of 3° towards the [110] direction. Further, the RWA facets are anti-reflection coated on both sides. The reflectivities of the RWL are chosen to achieve the same power density and current density as in the seeded RWA. Details of both designs are compiled in the next sections.

2.2 Device processing

We fabricated the III-V-semiconductor laser crystals on 3-inch wafers of n-GaAs substrate in a metalorganic chemical vapor deposition (MOCVD) reactor of our materials technology department, processed the wafers by standard lithography, reactive ion etching, implantation, deposition techniques for metals and dielectrics, and wafer thinning down to $120 \mu\text{m}$ (residual thickness) in our processing labs, cleaved and passivated the (110) laser mirror facets by two process variations: first by cleaving the substrate in air, cleaning it with atomic hydrogen in ultra-high vacuum (UHV) and depositing ZnSe onto the cleaved facets by molecular beam epitaxy (MBE). The second passivation technique was done by cleaving the crystal inside the UHV, followed by MBE-deposition of single-crystalline ZnSe onto the (110) facets of the cleaved laser bars without any exposure to the atmosphere [5]. Laser facet passivation is necessary in order to suppress catastrophic optical mirror damage (COMD). The COMD is attributed to originate from oxidation mainly of the aluminum-compound in the AlGaAs waveguide layer when exposed to air [6]. Anti- and high-reflection mirror coatings of dielectric quarter wave stacks were deposited onto the passivated facets in high-vacuum by ion beam deposition. Reflectivities of $R_f = 1\%$ at the front facet and $R_b = 98\%$ at the back facet were realized for the lasers, and $R < 0.1\%$ for the optical amplifiers.

After mirror deposition onto the laser bars, the individual laser diodes were electro-optically measured, inspected and selected for assembly. The laser diodes were soldered with AuSn hard solder (ζ -phase) p-side up onto AlN insulating submount. The submounts were soldered onto C-mounts made of Au-plated Cu, acting as heat spreader, for handling, and for providing the electrical contact interface. The laser chips were bonded with Au-wires for the p-contacts.

2.3 Epitaxial layer structure and laser chip dimensions

Two III-V heterostructure variants were used: one single quantum well and one double quantum well layer structure, both embedded in an asymmetric large optical cavity as (vertical) waveguide [7]. Each quantum well (QW) consisted of a 6 nm thick compressively strained InGaAs layers with 28% In-content, embedded in strain compensating GaAsP barriers.

Table 1. Design variants including epitaxial structures and lateral design.

No	Epi design	Lateral design	Straight section	Tapered section	Passivation
1	SQW	RWTL ₁	$L_{RW} = 4$ mm	$L_{TP} = 2$ mm	Cleaved in air
2	SQW	RWTL ₂	$L_{RW} = 2$ mm	$L_{TP} = 4$ mm	Cleaved in air
3	DQW	RWTL ₁	$L_{RW} = 4$ mm	$L_{TP} = 2$ mm	Cleaved in UHV
4	DQW	RWTL ₂	$L_{RW} = 2$ mm	$L_{TP} = 4$ mm	Cleaved in UHV
5	DQW	RWL	$L_{RW} = 6$ mm	$L_{TP} = 0$	Cleaved in UHV

The $\text{Al}_{0.25}\text{Ga}_{0.75}\text{As}$ confinement layers were $2.4\ \mu\text{m}$ thick for the SQW with a p:n thickness ratio of 1:2 and $4.8\ \mu\text{m}$ thick for the DQW having a 1:5 ratio in the p- versus n-layer thicknesses. Asymmetric large optical cavity design was used providing small internal loss for the optical field. In order keep the operational stress small, the device was relatively long, $L = 6\ \text{mm}$, and the stripe relatively wide, $w = 5\ \mu\text{m}$ (compared to a low-power RW laser design). Another longitudinal variant was chosen, aimed at further diluting the power density towards the front facet, where it reaches its maximum in the amplifier and in the laser due to the asymmetry in reflectivity for the latter. A tapered section was designed with $5\ \mu\text{m}$ stripe width starting at the back facet over a length of $L_{\text{RW}} = 4\ \text{mm}$ (variant RWTL_1) or $L_{\text{RW}} = 2\ \text{mm}$ (variant RWTL_2), followed by a linear and symmetric increase in lateral size from $5\ \mu\text{m}$ to $15\ \mu\text{m}$ at the front facet over a length of $L_{\text{TP1}} = 2\ \text{mm}$ or $L_{\text{TP2}} = 4\ \text{mm}$, for variants RWTL_1 and RWTL_2 , respectively. We investigated the five design variants listed in Table 1, two of them having single quantum well and tapered sections, and three having a double quantum well, two of them with taper and one with straight resonator (RWL). The variants no. 1 and 2 were passivated after cleaving in air, whereas no. 3 to 5 were processed using the UHV-cleaving.

2.4 Electro-optical characterizations

The light-current (LI-) characteristics of a straight $w = 5\ \mu\text{m}$ wide, $L = 6\ \text{mm}$ long ridge waveguide amplifier, seeded by a DBR laser, stabilized at $\lambda = 1064\ \text{nm}$ wavelength, is shown in Fig. 1. The light from the strained single InGaAs quantum well (design version no. 5, Tab. 1) is mainly linearly polarized in transverse electrical (TE) direction. The TE-polarized fraction of optical power was measured behind a polarization filter. All data were measured on our “breadboard”, i.e. with all components mounted on an optical table. The seed power was $P_{\text{seed}} = 16\ \text{mW}$, chosen to pump the RWA close to gain saturation, i.e. increasing the seed power would not increase the amplified power significantly. The TE-polarized power reaches almost $0.9\ \text{W}$ at $1.5\ \text{A}$ drive current through the RWA gain section. The fraction of power polarized perpendicular to TE was about 5%. The optical spectrum measured at a resolution bandwidth of $0.1\ \text{nm}$ at $I_{\text{RWA}} = 1.5\ \text{A}$ drive current through the RWA is plotted as red curve (Fig. 1, right). The spectrum is located on top of the amplified spontaneous emission (ASE) spectrum at maximum gain, as seen in the spectral part below $-30\ \text{dB}$, i.e. there is no detuning observed between gain maximum and seed wavelength ($1064\ \text{nm}$). The light-current-voltage (LIV) characteristics and the spectral map of a typical laser diode of design no. 5 (straight RWL) are indicated in Fig. 2. The optical power (blue curve) enters the thermal roll-over regime above $3.5\ \text{A}$; below that range it is thermally bent from a straight line above threshold current $I_{\text{th}} \sim 0.1\ \text{A}$. The LI-curve of the MOPA from Fig. 1 is plotted as green curve for comparison. Note, that the TE-polarized MOPA power is about 10% below the laser power, at least in the region above $1\ \text{A}$. This drop originates from power-dependent polarization loss, mainly by the polarization filter used for the measurement. The optical laser spectrum is above $1070\ \text{nm}$, shifted towards lower energy (longer wavelength) due to decreased carrier density compared to the amplifier design, where the ASE peak was close to $1064\ \text{nm}$ (Fig. 1). The optical spectrum and its center wavelength indicate a red shift (towards long wavelength) when increasing the current.

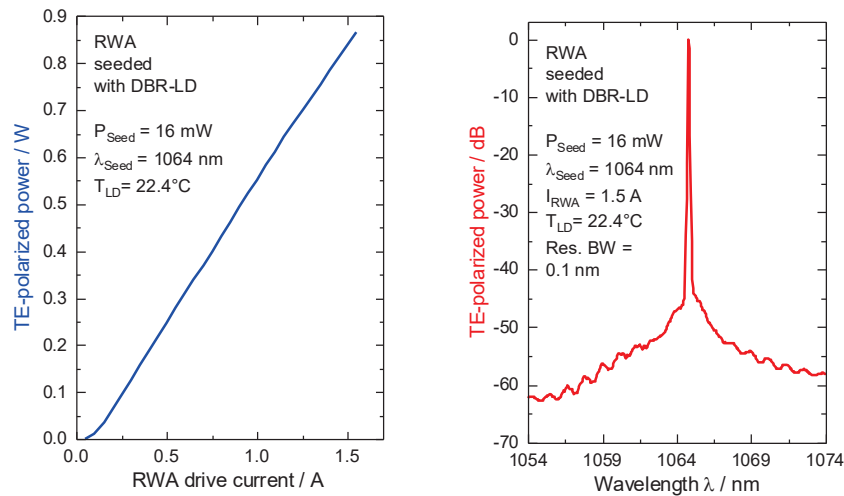


Figure 1. LI-curve (blue) and optical spectrum (red) of a typical DQW RWA seeded by a DBR laser diode at $\lambda = 1064\ \text{nm}$.

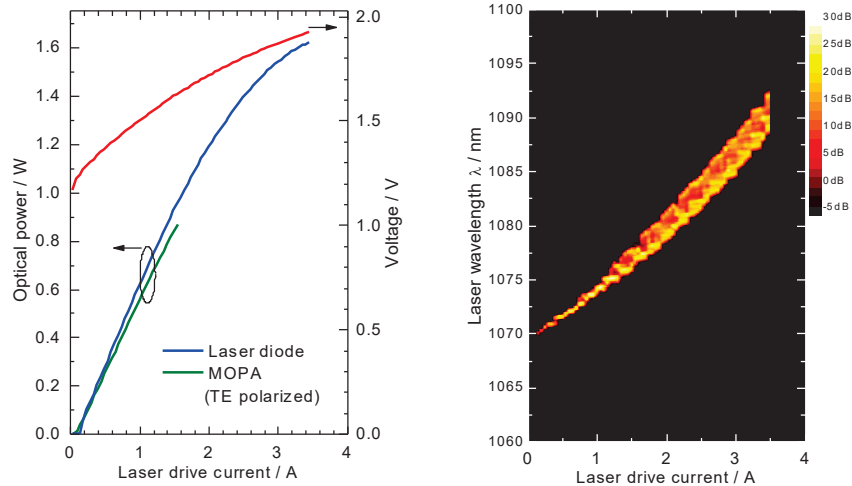


Figure 2. LIV-curves (blue, red) and spectral map (right plot) of a typical DQW RWL from the same batch as the RWA (green).

This shift is due to self-heating of the active zone with an approximate linear temperature increase as function of the dissipative (heat) power $P_w = U \times I - P$, at optical power P , voltage U and current I , and due to the temperature dependence of the energy gap. The latter was determined by measuring the LIV and spectral maps at different submount temperatures, here $T_{sub} = 20^\circ\text{C}$, 25°C and 30°C . The increase in temperature $\Delta T = R_{th} \times P_w$ in the active zone is linearly approximated by the thermal resistance R_{th} between active zone and submount. Evaluation of the temperature-dependent data for each laser results in a thermal resistance $R_{th} = 9.4 \pm 0.6$ K/W ($\pm 3 \times$ standard deviation) for design no. 5. Design no. 5 meets the requirements for BECCAL regarding the electro-optical performance. The other design variants (RWTL, no. 1 to no. 4) show even better performance with respect to the electro-optical data (due to higher gain). However, the design no. 5 has a much better reliability regarding operational life time than the other variants. This will be shown in the next sections.

2.5 Accelerated aging experiments

In the first step we used the single quantum well design (no 1 to 3, Tab. 1) for lifetesting. Lot-wise time-accelerated aging experiments were designed, simulated and performed in order to investigate the influence of power, current and temperature on the (statistical) distribution of sudden failures, gradual degradation and degradation-related failure events. The influence of stress on the growth rate of defects can be described by the model of “scale-accelerated failure time” with the Eyring stress function adapted for laser diodes:

$$t_{op} = \pi_{ac} t_{ac} \quad \pi_{ac} \propto I^m P^n \exp\left(-\frac{E_A}{k_B T}\right) \quad (1)$$

Where t_{op} is the operating time, t_{ac} is the aging time scaled by the acceleration factor π_{ac} with stress originating from the current I , power P and temperature T in the active region; m and n are the stress exponents of current and power, respectively, E_A is the thermal activation energy for defect generation and k_B is the Boltzmann constant. The temperature in the active region T is related to the temperature at the submount T_{sub} via the thermal resistance R_{th} (see also previous section):

$$T = T_{sub} + R_{th}(U \times I - P) \quad (2)$$

Selection of lots and stress factors were computed by Monte-Carlo simulations of log-normally distributed failure events using above acceleration model. The guidelines were:

- maximum of information at given test time and given sample count, here 15 lasers, $t = 2200$ h (3 months),
- close to 100% failures in the lots with highest stress,
- few survivals in the lot with lowest stress.

Table 2. Conditions and lasers for lifestest of standard passivated SQW of designs no. 1 (RWTL₁) and no. 2 (RWTL₂).

Lot	Design	Power P	Temperature		# LDs
			at submount	in active region	
1a	RWTL ₁	1.2 W	T _{sub} = 25°C	T = 34°C	2
1b	RWTL ₂	1.4 W	T _{sub} = 25°C	T = 38°C	3
2	RWTL ₂	1.7 W	T _{sub} = 20°C	T = 38°C	5
3	RWTL ₂	1.7 W	T _{sub} = 30°C	T = 48°C	5

Details of test optimization are beyond the scope of this paper [8]. Here, we show the result of the four-lot test with the stress conditions listed in Tab. 2.

The maximum optical power (1.7 W) was chosen well below the thermal roll-over of the RWTL (more than 2.2 W). The lifestest plot of the first test run is depicted in Fig. 3. During the initial 168 h (1 week) the lasers were subjected to burn-in at 25°C, 1.2 W. Burn-in is required in order to wipe out any initial failures. The burn-in conditions were selected following the experience from former tests. Here, all devices survived the burn-in without any detectable degradation. After burn-in the devices are viewed as “screened” in initial condition ($t_{op} = 0$).

The test was finished after 2336 h, i.e. 2168 h after burn-in. Two devices of Lot 1 were still operational after the life test, the other 13 lasers totally failed as indicated by the rapid increase in drive currents at constant optical powers. At highest stress, lot 3: 30°C, 1.7 W, all lasers failed until 335 h, counted after burn-in, i.e. within two weeks of accelerated stress. At the next lower stress level, lot 2: 20°C, 1.7 W, all lasers failed until 1145 h after burn-in. The power level of lot 1b was chosen to reach the same thermal stress as in lot 2. The differences in lifetime (failure rate) among lots 1b and 2 are thus attributed to stress by optical power (and/or current), but not by temperature. The differences in failure rate between lot 2 and lot 3 are mainly due to the temperature difference of 10 K, but not by optical power.

Visual inspections and electro-luminescence imaging after life test revealed, that all failed devices degraded by catastrophic optical mirror damage (COMD). Since COMD is usually attributed to local temperature enhancement triggered by non-radiative surface-recombination, followed by optical absorption at the front facet (mirror), the COMD degradation depends on the optical power density at the front facet, rather than the current through the device.

More information about the actual degradation mechanism can be obtained by evaluating the LIV curves, measured after each 100 h during aging in automated mode. For one laser the LIV data show a significant degradation; the other lasers degraded too fast within the period of 100 h for any detectable change in the LIV characteristics. Figure 4 shows the LIV curves (4a) of the respective laser diode of lot 1 b (arrows in Fig. 3), and threshold current I_{th} and slope efficiency S_{th} with offset $P_{th} = I_{th} \times S$ computed from linear fit around laser threshold (4b). After 500 h to 700 h the threshold current continuously increases and an ongoing drop in slope efficiency is observed.

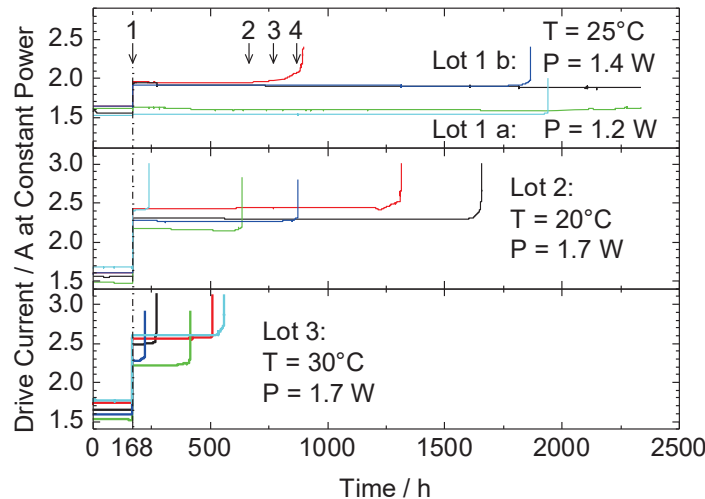


Figure 3. Accelerated life test plots of LDs, var. 1, in 4 lots, each at different (T, P). Automated LIV-measurements were made after each 100 h for each LD. Degradation in LIV was spotted four times (1-4) for one LD (red curve).

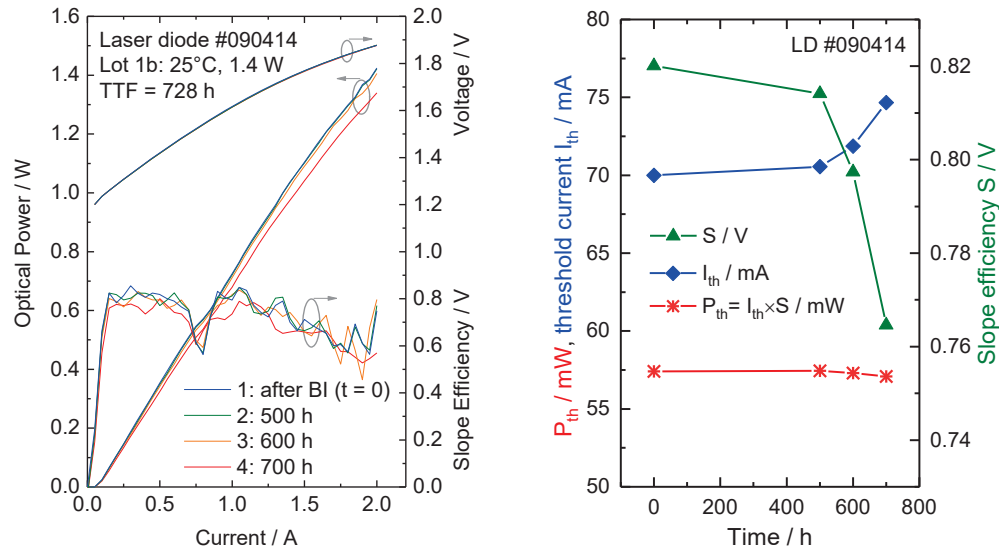


Figure 4. a) Left: Evolution of LIV curves. b) Right: threshold current I_{th} , slope efficiency S , and power $P_{th} = I_{th} \times S$ of one LD from lot 1 at four spots measured during aging (cf. Fig 3).

The offset P_{th} is almost constant within accuracy of measurement. Since both I_{th} and S depend on the internal (quantum) efficiency η_i as $I_{th} \sim 1/\eta_i$ and $S \sim \eta_i$, the offset power P_{th} does not depend on η_i . The decrease in η_i during the last 200 hours before COMD reflects the role of non-radiative surface-current at the front facet leading to COMD. Since P_{th} depends on the fundamental laser diode parameters according to eq. 3:

$$P_{th} = \hbar\omega V B N_{tr}^2 F_f \frac{\alpha_m}{\alpha_i + \alpha_m} \exp\left(2 \frac{\alpha_i + \alpha_m}{\Gamma g_0}\right), \quad (3)$$

it is concluded that the internal (photon) loss α_i , as well as the other active-material dependent parameters: bimolecular recombination coefficient B , transparency carrier density N_{tr} , reflectivity R_f of front- and R_b of back-facet in $F_f = 1/(1 + \sqrt{R_f/R_b}(1 - R_b)/(1 - R_f))$ and mirror loss $\alpha_m = -\log(R_f R_b)/2L$, and the confined gain coefficient Γg_0 most probably are not affected by aging within the detection limits of measurements ($\hbar\omega$ is the photon energy, V is the volume of the active region).

The lifetest of air-cleaved, H+-cleaned and ZnSe-passivated lasers of design variants 1 and 2 revealed that this passivation method was not suited to significantly suppress the rapid and sudden degradation modes caused by COMD in our 1064 nm laser diodes at given high-stress levels over 2000 hours.

In view of this result, a second batch of laser diodes was manufactured using passivation by UHV-cleaving. This time, double quantum well lasers were used including the former lateral design variants (RWTL₁ and RWTL₂ acc. Tab. 1). In addition, RWL without taper were tested. The lifetest was performed at $T = 25^\circ\text{C}$ submount temperature. The RWTL were tested at 1.7 W, the RWL at 1.5 W, about 10% below the thermal roll-over (cf. Fig 1) Initially, 8 laser diodes of RWL design (no. 5) and 8 laser diodes of RWTL design were subjected to burn-in, 5 of them with design variant no. 3, three of design no. 4. (Tab. 1). One RWL was rejected due to thermal roll-over close to 1.5 W. One RWTL of design variant no. 4 failed during burn-in at 40 h by rapid degradation without facet damage. The lifetest plot of the burn-in qualified 14 laser diodes is shown in Fig. 5.

There was no failure among the RWL (lot 5, upper plot) until 3750 hours and one sudden failure at 3755 h. Only 1 laser of 7 snapped until the end of the lifetest of lot 5 (5050 h – 5280 h). Visual inspections and electroluminescence (EL) showed no COMD or any other peculiarity related to facet degradation. The batch of RWTL indicated 6 failures out of 7; one RWTL of design no. 4 was still operational after end of the test (5050 h). All failures were due to sudden failure events without any indication of gradual degradation. As indicated by visual inspections and EL, there was no single COMD, nor any hint on the failure cause. Destructive investigations by cathodoluminescence (CL) imaging of the failed lasers in top-view (i.e. perpendicular to the epi-layers) could not clearly identify the root cause of total failure.

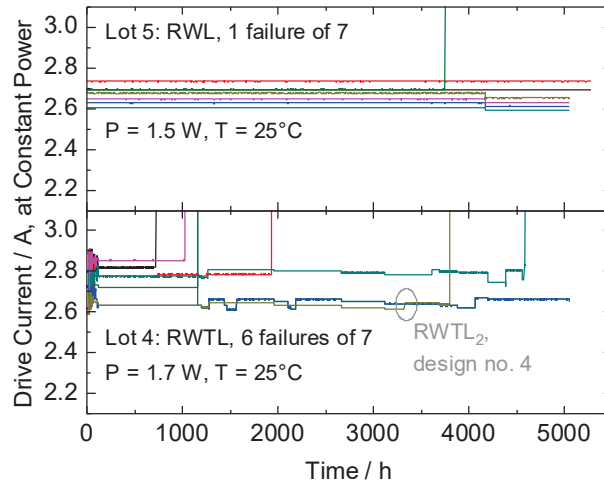


Figure 5. Accelerated life-test plots of RW LDs without taper, design no. 5 (upper plot) and with taper, design no. 3 (five lasers) and no. 4 (two lasers) in the lower plot.

There were some dark spot defects (DSD) randomly distributed along the waveguide which are typical for gradual degradation of the interior region apart from the surface. But, we could not find any dark line defects typical for COD. The origin of sudden failures in this case was not clear and it will be subject of further investigations.

To summarize this section, we demonstrated that COMD was totally suppressed in 1064 nm laser diodes by applying an improved process for facet passivation. Cleaving in UHV instead of cleaving in air prior to ZnSe epitaxy on the cleaved facet successfully prevents the laser mirror from oxidation and subsequent degradation by operational stress. Any failures in UHV-cleaved passivated lasers occur considerably later and they are not related to facet degradation. There is obviously another, still unidentified design-related failure source attributed to the tapered RW lasers, causing sudden failure associated with some internal dark spot defects. UHV-cleaved passivated straight RW lasers without taper resulted in the longest lifetime at highest applicable power close to thermal roll-over.

3. EVALUATION OF LIFETEST DATA

As presented in previous section, we subjected ridge waveguide laser diodes with different process and design variants to accelerated aging experiments. In the first lifetest, only tapered ridge waveguide lasers (RWTL) from the same manufacturing lot with qualified processes were used. Those lasers differ only in the length of the taper section, otherwise they are identical, especially regarding the extension of the optical field at the laser facets. The failure cause was related to non-radiative surface recombination followed by optical absorption, heating up the facets dependent on the optical output power rather than the current flow through the laser stripe. Using the model of scale-accelerated failure time (eq. 1) it is reasonable to neglect the current stress exponent $m = 0$, and to consider power stress and thermal activation ($n > 0$, $E_A > 0$). Further, any differences in the taper section length should not affect the facet degradation (considerably) and are therefore neglected. In addition, we use the log-normal function as statistical distribution of failure time. Under those assumptions the negative log-likelihood of the observed failure events is:

$$-\log \mathcal{L} = \sum_{i=1}^N \Lambda(\pi_i t_i) - \sum_{i=1}^k \log \pi_i \lambda(\pi_i t_i), \text{ where}$$

$$\Lambda(t) = -\log \left[\Phi_{norm} \left(\frac{\log(t) - \mu}{\sigma} \right) \right], \text{ and } \lambda(t) = \frac{1}{\sigma t} \exp \left[\Lambda(t) - \frac{1}{2} \left(\frac{\log(t) - \mu}{\sigma} \right)^2 \right] \quad (4)$$

with the location and scale parameters μ and σ , respectively, and acceleration factors π_i as defined in eq. (1) for device no. i at time t_i , and k failures of N components.

Table 3. Maximum-likelihood estimate and confidence intervals based on likelihood profiling.

Parameter	ML estimate	Confidence limits	
		80%	20%
n	5.45	3.62	7.39
E_A / eV	0.80	0.41	1.18
μ	10.7	9.59	11.8
σ	0.89	0.76	1.06
R(10 kh)	95.0%	66.3%	99.8%

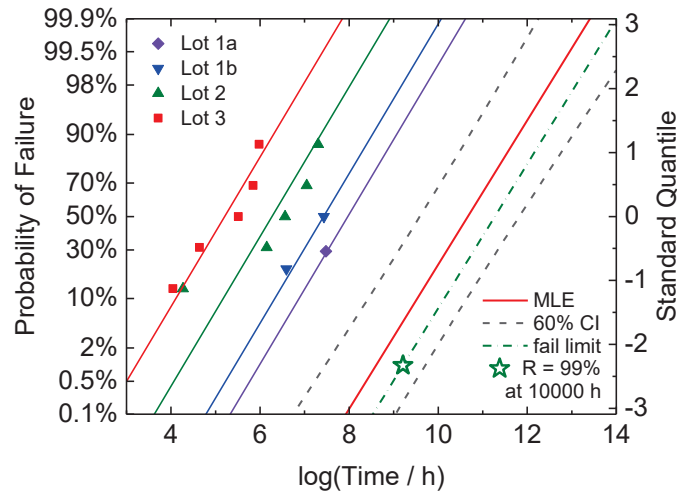


Figure 6. Evaluation of lots 1 to 3: TTFs are shown as dots on a log - probability plot. Maximum-likelihood estimate (MLE) of failure function and 60% the confidence interval (CI) at operating conditions are indicated. MLE is before the fail limit.

Minimizing $-\log\mathcal{L}$ results in the maximum-likelihood (ML) based estimates for the acceleration parameters n , E_A and the distribution parameters μ and σ , and their confidence intervals, latter by profiling the likelihood, for example. Evaluating the data using the software “R” yields the results listed Tab. 3. As a result, the ML estimate for the reliability R(10 kh) over 10,000 hours is 95%, and its lower 80% confidence limit is 66%, thus this batch does not meet the specifications (design versions no. 1 and 2).

For graphic illustration the results are plotted in Fig. 6. The point-estimate of failure probability is plotted against logarithm (base e) of failure time in hours in a log-normal probability plot. Standard-quantiles are the inverse of the normal-distribution, thus giving straight lines for the fitted curves $y = (\log(t) - \mu)/\sigma$, with slope $1/\sigma$ and 50%- (mean-) value μ . The colored straight lines fitting the failure points indicate the maximum-likelihood results for the respective failure distribution of each lot i with relative 50%-locations at $\mu_i = \mu - n \log(P_i/P_{op}) + E_A/k_B T_i - E_A/k_B T_{op}$.

At operating point (0.83 W, 25°C) the red line on the right side marks the failure probability under device operation. The pass criterion $R > 99\%$ at 10 kh (green star) is not reached by the red curve, although the pass criterion is within the 60% confidence band (pointwise confidence intervals of R). This reflects the high risk of using such material for lasers or amplifiers for continuous operation over 10,000 hours.

Table 4. ML estimate and CI for R(10 kh), median lifetime (MLT) and mean time to failure (MTTF) for Lot 4 (RWTL)

Reliability measure	ML estimate	Confidence Intervals					
		0.5%	5%	20%	80%	95%	99.5%
R(10 kh)	100.00%	97.80%	99.93%	100.00%	100.00%	100.00%	100.00%
MLT / h	9.3E+5	3.4E+5	5.4E+5	7.2E+5	1.2E+6	1.7E+6	3.0E+6
MTTF / h	1.3E+6	5.8E+5	7.7E+5	9.6E+5	1.9E+6	3.4E+6	1.5E+7

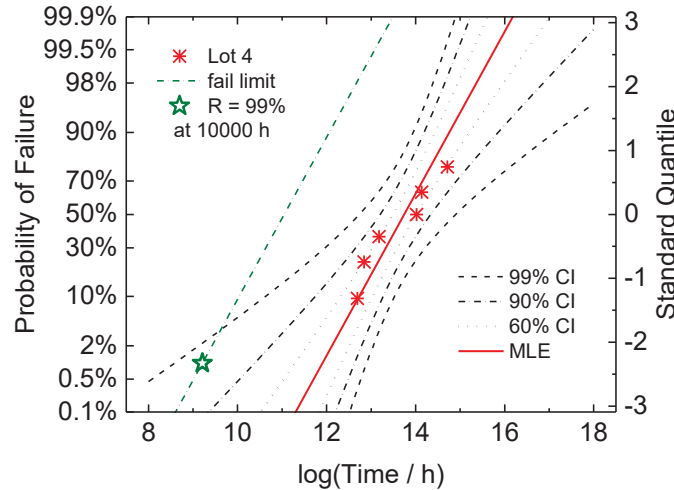


Figure 7. Evaluation of lot 4: TTFs are shown as stars on a log - probability plot. Maximum-likelihood estimate (MLE) of failure function and 60 - 99% the confidence intervals (CI) at operating conditions are indicated. The R = 99% point at 10,000 h is inside the 99% CI. MLE is after the fail limit.

As motivated in section 4 (discussions), we assume the same thermal activation energy and the same power stress exponent for the design variants no. 3 to 5 as for no. 1 and 2. With those assumptions, the lifestest data of the lots 4 and 5 were evaluated. By maximizing the likelihood with respect to the location and scale parameters (μ , σ) and computing its profile, the values listed in Table 4 and plotted in Fig. 7 are obtained for Lot 4 (RWTL).

The fitted values were $\mu = 13.7$ and $\sigma = 0.79$. With those values the median life time (MLT) and mean time to failure (MTTF) are given as $MLT = \exp(\mu)$ and $MTTF = \exp(\mu + \sigma^2/2)$. Note, that the reliability is close to 100% and MTTF and MLT are in the range of 1 million hours, exceeding the specification by far. There is some residual, $\alpha = 0.5\%$, risk of $R \leq 97.8\%$ for the reliability of UHV-cleaved passivated RWTL at operating conditions, acc. to the data listed in Tab. 4. This residual risk is also depicted in Fig. 7. Evaluation of the single failure in lot 5 was done at constant $\sigma = 0.79$, obtained from lot 4, since one failure allows only for fitting one parameter, which reasonably is the location μ .

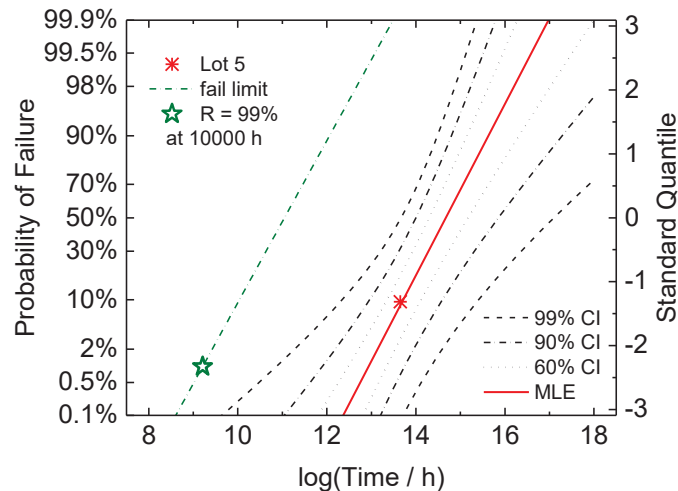


Figure 8. Evaluation of lot 5 with same notations as for lot 4: MLE and CI's were computed from the joint likelihood of both lots at constant σ . The 99% CI is beyond the R = 99% limit at 10,000 h.

Table 5. ML estimate and CI for R(10 kh), median lifetime (MLT) and mean time to failure (MTTF) for Lot 5 (RWL).

Reliability measure	ML estimate	Confidence Intervals					
		0.5%	5%	20%	80%	95%	99.5%
R(10 kh)	100.00%	99.96%	100.00%	100.00%	100.00%	100.00%	100.00%
MLT / h	2.5E+6	8.6E+5	1.2E+6	1.7E+6	3.8E+6	5.8E+6	1.0E+7
MTTF / h	3.4E+6	1.2E+6	1.7E+6	2.3E+6	5.1E+6	8.0E+6	1.4E+7

The result is $\mu = 14.7$. The confidence intervals are listed in Tab. 5 and depicted in Fig. 8. The $1 - 2\alpha = 99\%$ (both sided) confidence interval, i.e. the $\alpha = 0.5\%$ one-sided risk, is far beyond the pass-criterion $R(10\text{kh}) > 99\%$ (green star) for the UHV-cleave passivated RWL of lot 5. We therefore recommend to use this material as RWA for BECCAL.

4. DISCUSSION

4.1 Choice of epitaxial layer structures and laser design

Using asymmetric waveguide instead of symmetric ones has several advantages. Most important in terms of reliable device performance are the reduction of power density in the quantum well and on the p-side, while keeping the series resistance small without the necessity of increasing the doping concentration, which would in turn increase the internal optical loss by free-carrier absorption which would generate heat due to inelastic carrier scattering. Reducing the internal loss allows to increase the resonator length which results in further reduction of the carrier density and optical power density, and in the reduction of temperature in the active region. In terms of waveguiding, the extension of the optical field towards the n-side allows for larger stripe width for (nearly) single lateral mode operation compared to the symmetric case. Thermal stress, optical power, and current density should be as small as possible for a required output power, since those stress sources accelerate the growth of defects by thermal activation and energy dissipation, adversely affecting the device lifetime and reliability. In terms of reliability the use of an SQW instead of a DQW should be preferred for the following reasons. There is less heat generated and cooling is more effective in an SQW compared to a DQW, since the threshold current is smaller and the heat source is less spread in the SQW. In addition, the total strain energy is smaller in the SQW, providing less nucleation sites for any strain-relaxing (misfit) dislocations and/or formation of other crystal defects, such as interstitials or vacancies. Qualifying the DQW in terms of lifetime should therefore qualify the SQW at the same power density, provided that UHV-cleaved passivation will be used.

4.2 Choice of acceleration parameters and limits of predictability

To justify the evaluation of the second lifestest by using the acceleration parameters of the first lifestest, $E_A = 0.8$ eV and $n = 5.45$, some simplifying assumptions should be noted. The differences of both batches are as follows. First, a double quantum well was used for batch 2 (aging lots 4 and 5) causing higher (total) strain energy in the InGaAs quantum wells and GaAsP barriers, and a thicker heat source (each QW heats up its neighboring QW) compared to the single quantum well of previous batch 1 (aging lots 1 to 3). Second, the vertical confinement layer has double size ($4.8 \mu\text{m}$) in the DQW compared to the SQW ($2.4 \mu\text{m}$). Third, the facets do not have any oxide between ZnSe passivation layer and III-V active material. However, following arguments justify our approach. We attribute COMD to the mechanism of “non-radiative recombination-enhanced defect generation or multiplication” (REDG) [9]. Starting from point defects, such as interstitials, vacancies or impurities (including oxides at facet lattice sites), there is a certain amount of non-radiative current from Shockley-Read-Hall recombination causing energy dissipation, local heating and temperature raise. Non-radiative recombination thermally activates further generation of defects that may accumulate, forming dislocation loops (dark spot defects), finally leading to gradual degradation or COD by absorption, subsequent dark line formation and temperature increase, eventually up to the melting point of the material. REDG is therefore an intrinsic, material-dependent process, rather than a design related mechanism. Since the temperature rise in the DQW is attributed to the self-heating by means of the thermal resistance R_{th} , it is reasonable to use the degradation parameters n and E_A of the first batch for the second batch with respective thermal resistance, which was derived from the measurements of each laser diode. The same materials for chip processing, and the same III-V heterostructure compositions were used in both cases. We further neglect any other potential sources and attribute the sudden failures in the second batch to be caused by the same stress function as in the first batch.

Nevertheless, future lot-wise accelerated lifetests should be done with a sufficient number of samples from UHV-cleaved passivated RWL (design no. 5) to gain higher confidence in the prognosis on operational lifetime, especially for future satellite missions with operational lifetime exceeding 3 years.

5. SUMMARY, CONCLUSION AND ACKNOWLEDGEMENT

Long wavelength III-V semiconductor quantum well lasers beyond the $\lambda = 980$ nm limit (EDFA pumps) are known to be prone to degradation and sudden failure due to facet oxidation and the impact of increased strain energy when increasing the In-mol fraction in the highly strained InGaAs quantum well. In this contribution we presented a suited combination of large optical cavity laser design, wafer epitaxy, processing, passivation and assembly to gain laser material that is robust against failure when operating continuously at 1064 nm wavelength with around 0.8 W optical power over 10,000 hours. Failure-time accelerated lifetesting results in an estimate of thermal activation energy $E_A = 0.8$ eV and power stress exponent $n = 5.45$ for 1064 nm lasers that degraded by COMD. With those parameters, the reliability of ridge waveguide lasers with COMD suppressed by an improved passivation technique was estimated to be close to 100%. We recommend to use this qualified material and our qualified processes for ridge waveguide amplifiers (RWA) in the BECCAL modules for the optical dipole trap lasers.

The authors would like to thank Sabrina Kreutzmann for chip assembly, Helen Lawrenz for CL investigations, Sabine Ullrich and Maik Erbe for lifetest measurements, Christof Henze for electro-optical measurements, and the BECCAL-team for working together, sharing knowledge and collaborating. This work is supported by the German Space Agency (DLR) with funds provided by the Federal Ministry for Economic Affairs and Climate Action (BMWK) due to an enactment of the German Bundestag under grants no. 50WP1704 and 50WP2104.

REFERENCES

- [1] Frye, K., Abend, S., Bartosch, W. et al., "The Bose-Einstein Condensate and Cold Atom Laboratory," EPJ Quantum Technology 8, 1 (2021).
- [2] Schlippert, D., Hartwig, J., Albers, H., Richardson, L.L., Schubert, C., Roura, A., Schleich, W.P., Ertmer, W., and Rasel, E.M., "Quantum test of the universality of free fall," Phys. Rev. Lett. 112, 203002 (2014).
- [3] Gaunt, A. L. Schmidutz, T. F. Gotlibovych, I, Smith, R. P., and Hadzibabic, Z., "Bose-Einstein Condensation of Atoms in a Uniform Potential", Phys. Rev. Lett. 110, 200406 (2013)
- [4] Häusler, K., Staske, R., Maaßdorf, A., Ressel, P., Stölmacker, C., Tränkle, G., and Crump, P., "Pulsed Diode Laser Minibars for Pumping Space-Borne Solid-State Lasers," IEEE Photon. Tech. Lett. 33 (17), 963-966 (2021).
- [5] Boschker, J.E., Spengler, U., Ressel, P., Schmidbauer, M., Mogilatenko, A., "Stability of ZnSe-passivated laser facets cleaved in air and in ultra-high vacuum," IEEE Photonics Journal 14 (3), 1-6 (2022).
- [6] Tomm, J. W., Ziegler, M., Hempel, M., and Elsaesser, T. "Mechanisms and fast kinetics of the catastrophic optical damage (COD) in GaAs-based diode lasers," Laser & Photonics Reviews 5(3), 422-441 (2011).
- [7] Wenzel, H., Bugge, F., Dallmer, M., Dittmar, F., Fricke, J., Hasler, K. H., and Erbert, G., "Fundamental-Lateral Mode Stabilized High-Power Ridge-Waveguide Lasers with a Low Beam Divergence", IEEE Photon. Tech. Lett. 20 (3), 214-216 (2008).
- [8] Meeker, W.Q., and Escobar, L.A., Statistical Methods for Reliability Data, 2nd ed. NY, Wiley, 289-306 (2022)
- [9] Chuang, S.L., Nakayama, N., Ishibashi, A., Taniguchi, S., and Nakano, K., "Degradation of II-VI blue-green semiconductor lasers", IEEE Journal of Quantum Electronics 34 (5), 851-857 (1998).